nature materials

LETTERS
https://doi.org/10.1038/s41563-019-0391-7

Cellular nanoscale stiffness patterns governed by intracellular forces

Nicola Mandriota[1], Claudia Friedsam[2], John A. Jones-Molina[1], Kathleen V. Tatem[1,3], Donald E. Ingber[2,4,5] and Ozgur Sahin[1,3]*

Cell stiffness measurements have led to insights into various physiological and pathological processes[1,2]. Although many cellular behaviours are influenced by intracellular mechanical forces[3–6] that also alter the material properties of the cell, the precise mechanistic relationship between intracellular forces and cell stiffness remains unclear. Here we develop a cell mechanical imaging platform with high spatial resolution that reveals the existence of nanoscale stiffness patterns governed by intracellular forces. On the basis of these findings, we develop and validate a cellular mechanical model that quantitatively relates cell stiffness to intracellular forces. This allows us to determine the magnitude of tension within actin bundles, cell cortex and plasma membrane from the cell stiffness patterns across individual cells. These results expand our knowledge on the mechanical interaction between cells and their environments, and offer an alternative approach to determine physiologically relevant intracellular forces from high-resolution cell stiffness images.

Mechanical properties of cells are important regulators of physiology, organ development and disease[3,4,7]. As a probe of mechanical properties, cell stiffness measurements typically treat cells as passive isotropic materials[8], although cells are both anisotropic and actively prestressed by tensional forces that are generated within the cytoskeleton and transmitted throughout its volume[7,9]. Because of the small physical dimensions of the structures involved in force generation and transmission (for example motor proteins, cytoskeletal filaments and the plasma membrane), it is difficult to relate cell stiffness to specific intracellular forces, except for special cases where a single force component dominates the cell mechanical behaviour[2]. Imaging of cell stiffness with an atomic force microscope (AFM)[10,11] could potentially discriminate signatures of intracellular forces, if sufficient sensitivity and spatial resolution are achieved. Topographic images obtained with an AFM can resolve many subcellular structures with nanoscale resolution[12]; however, it has been difficult to perform mechanical characterization of these structures at this scale. Developments in multifrequency and peak-force AFM methods[13,14], as well as the use of high-bandwidth cantilevers[15], promise significant improvements in the resolution of cell stiffness images, but these methods still interpret measurements using models that do not account for cellular prestress. Hence, the relationship between stiffness and intracellular forces remains elusive. Here we present cell mechanical measurements with a novel AFM-based method that revealed a mechanistic link between intracellular forces and cell stiffness at the nanoscale. We first describe the method and compare nanoscale stiffness images with fluorescence images to observe the nanoscale effects of cytoskeletal forces. We then use patterns found in stiffness images to develop and validate a mechanical model that links intracellular tensional forces to cell stiffness.

To obtain high-resolution stiffness images of cells with an AFM, we adapted T-shaped cantilevers[16] for cell stiffness imaging. T-shaped cantilevers can measure tip–sample forces in tapping mode using torsional vibrations due to the fast response speed and high deflection sensitivity of torsional vibrations. With T-shaped cantilevers designed for cell stiffness imaging (Supplementary Fig. 1), force–distance curves can be obtained with unprecedented reductions in cellular indentations (down to 20 nm), and with force noise less than 10 pN root mean squared (Methods). These high-speed force curves exhibit little hysteresis (Fig. 1a), suggesting that the response of the cell at the nanoscale is only slightly viscoelastic.

As a first step, we used the Derjaguin–Muller–Toporov (DMT) contact mechanics model (Methods) to analyse the force curves and generate effective elastic modulus images of cells. Figure 1b–f shows images of a variety of living cells, including melanoma cells, fibroblasts, human umbilical vein endothelial cells (HUVECs) and Chinese hamster ovary (CHO) cells. These images revealed a richness of nanometre- to micrometre-sized features that correspond to focal adhesions and actin filaments (either alone or within bundles) on the basis of their morphology and of comparisons with fluorescence microscopy images. In particular, rod-like stiff elements, which might be single actin filaments, were clearly resolved despite being only 30 nm apart (Fig. 1f), which to our knowledge is unprecedented in the context of live-cell stiffness imaging. Note that the DMT model does not account for intracellular forces and substrate effects, and these limitations could cause effective elastic modulus values to vary significantly. Yet, these images provide a useful starting point to develop a more comprehensive model, by demonstrating the high spatial resolution and making comparisons with fluorescence images of load-bearing cytoskeletal components.

By fluorescently tagging cytoskeletal components of live fibroblast cells in parallel fluorescence microscopic images, we were able to confirm that focal adhesions invariably correspond to stiffer regions (Fig. 2a–c), whereas microtubules, which are known to bear compression and buckle in physiological conditions in living cells[17], were confined to more compliant regions of the cytoplasm (Fig. 2d–f), and the boundaries between these microtubule-rich and deficient regions exhibited sharp stiffness transitions (Fig. 2f). Importantly, comparison of surface topography and stiffness

---

[1]Department of Biological Sciences, Columbia University, New York, NY, USA. [2]Wyss Institute for Biologically Inspired Engineering, Harvard University, Boston, MA, USA. [3]Department of Physics, Columbia University, New York, NY, USA. [4]Harvard John A. Paulson School of Engineering and Applied Sciences, Harvard University, Cambridge, MA, USA. [5]Vascular Biology Program and Departments of Surgery, Boston Children's Hospital and Harvard Medical School, Boston, MA, USA. *e-mail: sahin@columbia.edu

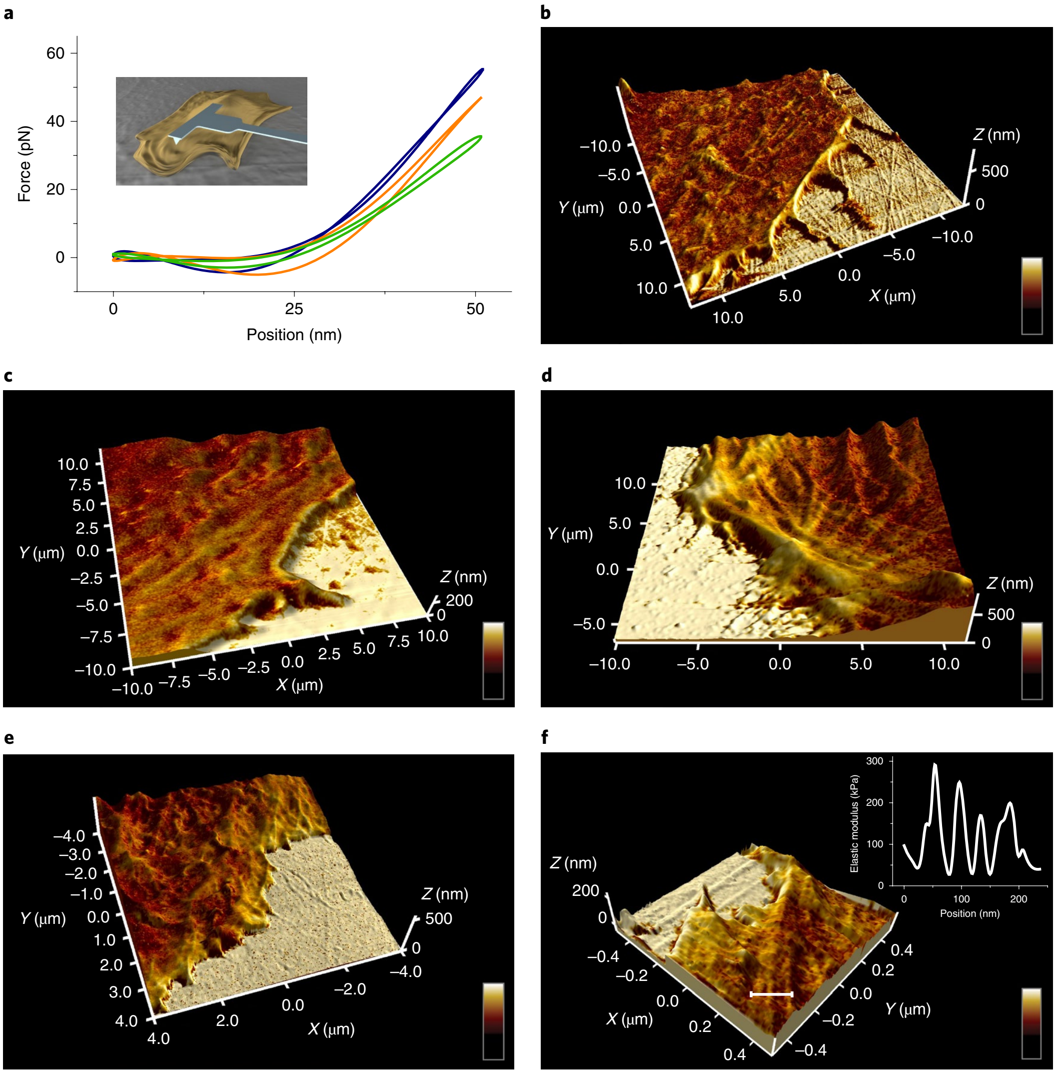

Fig. 1 | Imaging nanoscale stiffness of cells. a, Force versus distance curves acquired while scanning a living fibroblast show low imaging forces and depth of indentation. Inset: illustration of a T-shaped cantilever probing an adherent cell. **b–f**, Effective elastic modulus maps acquired from the periphery of living melanoma (**b**), HUVEC (**c**), fibroblast (**d**,**f**) and CHO cells (**e**). Effective elastic modulus values in logarithmic scale are colour-coded and superimposed on the surface topography. The elastic modulus profile (inset) across the dashed line in **f** shows clearly resolved features separated by 30 nm, which might be single actin filaments, according to their diameter and linearity. Colour bars are 9 to 140 kPa (**b**), 0.3 to 2.8 MPa (**c**), 12 to 370 kPa (**d**), 74 to 738 kPa (**e**) and 28 to 880 kPa (**f**).

measurements in these boundary regions revealed that there was no local change in cell thickness associated with the sharp stiffness transition (Supplementary Fig. 2), and thus the abrupt change in mechanics we measured appears to be due to local changes in cell mechanics in these regions.

Comparisons of stiffness images with the distribution of fluorescently tagged F-actin revealed that, although linear features in the stiffness images coincided with actin filaments and bundles (Fig. 2g–i, see also Supplementary Fig. 3 for a comparison near the leading edge), there was no apparent correlation between fluorescence intensity and stiffness of the bundles (Supplementary Fig. 4)[18]. We also observed cases in which the stiffness contrast varied markedly over time and when myosin II was inhibited with blebbistatin (Supplementary Figs. 5–9). Taken together, these observations support the previously suggested view that intracellular tensional forces and cytoskeletal prestress strongly affect cell stiffness[8,19], and justify the search for a mechanism that quantitatively relates stiffness to intracellular forces.

Importantly, in the course of these AFM studies, we noticed that the stiffness of curved actin bundles at the cell edge appears to correlate with their curvature radius (Fig. 3a). These peripheral bundles are a subset of stress fibres displaying distinct morphology, and their tension directly determines cell shape at the periphery[20,21]. Specifically, the curvature radius, R, of a bundle at the cell edge is linearly proportional to its tension, T, due to surface forces exerted by the plasma membrane[22] (Fig. 3b). Therefore, the observed correlation between stiffness and curvature offers the possibility to determine a mechanical model of the cell that can relate tension and stiffness.

We tested whether a simple model described by a tensioned beam resting on an elastic foundation (Fig. 3c) can quantitatively predict the correlation between stiffness and curvature radius. According

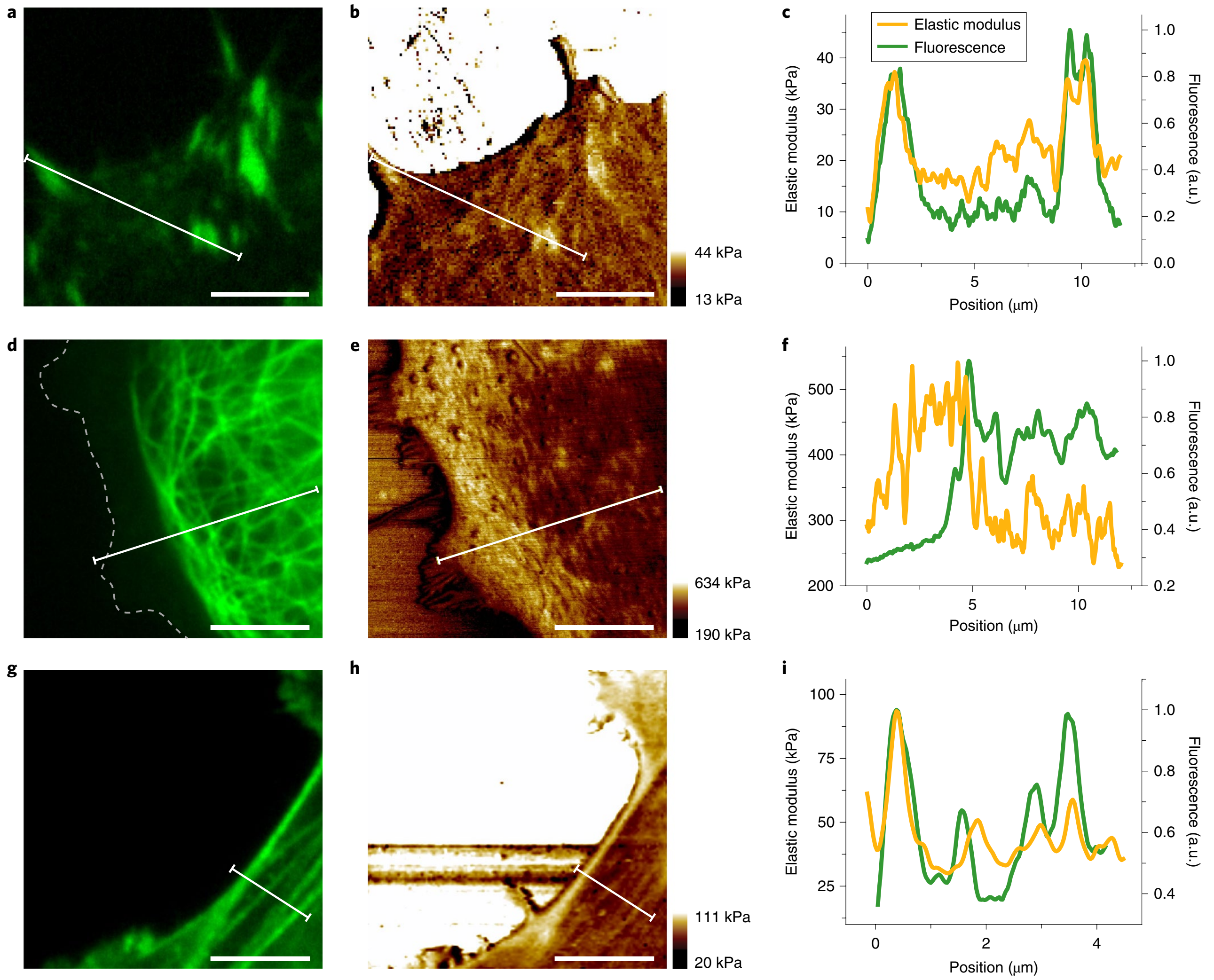

Fig. 2 | Stiffness of load-bearing cytoskeletal components. a–i, Living fibroblast cells are tagged with fluorescent talin (**a–c**), tubulin (**d–f**) or actin (**g–i**), and imaged with an AFM for stiffness. The left-hand panels are the fluorescence images, and the middle panels are the stiffness images. The graphs on the right compare fluorescence intensity and stiffness across the lines indicated on the respective images. The colour bars indicate effective elastic modulus values in a logarithmic scale. The horizontal feature to the left of the cell in **h** is an imaging artefact, possibly due to a temporary contamination of the tip, or due to noise or vibrations that are coupled to the microscope. Scale bars, 5 μm.

to this model, deformation of the beam by the AFM tip causes tensional forces to acquire a vertical component towards the tip, which increases with deformation. The model relates the AFM-measured stiffness k_b to T as follows:

$$k_b = 2\sqrt{TK_{1D}} \quad (1)$$

Here K_{1D} is the foundation modulus, which accounts for the interaction between the bundle and surrounding cytoskeleton (see Methods for derivation). Equation (1) predicts that in a given cell the square of bundle stiffness would scale linearly with curvature radius: $k_b^2 \sim R$. We tested this scaling behaviour using curvature and stiffness data obtained from 13 bundles in five cells, and validated the scaling prediction over a wide range of radii, from 3 to 50 μm (Fig. 3d). (See Methods for selection criteria of cells and details of data analysis.) As seen from these plots, linear trends fit well to the data (R^2 values greater than 0.97), which supports the conceptual model shown in Fig. 3c. (See Supplementary Note 1 for discussions on the predicted scaling behaviour when stiffness is dominated by the bending modulus of actin fibre bundles: $k_b^4 \sim R$. Data in Fig. 3d rule out this possibility.)

The model in Fig. 3c also predicts that there should be a finite mechanical coupling distance l_b, which specifies how far the effects of a force applied perpendicularly to a bundle will be transmitted along that bundle. The coupling distance can be observed experimentally near focal adhesions. If the focal adhesion is substantially stiffer than its neighbouring actin bundle, stiffness measured along the bundle can be expected to increase gradually towards the focal adhesion according to equation (8) in Methods. Consequently, stiffness gradients can be used to determine l_b, which is related to tension by

$$l_b = \sqrt{\frac{T}{K_{1D}}} \quad (2)$$

Figure 3e shows stiffness gradients along three bundles exhibiting a gradual increase in stiffness near focal adhesions. Fitting the data

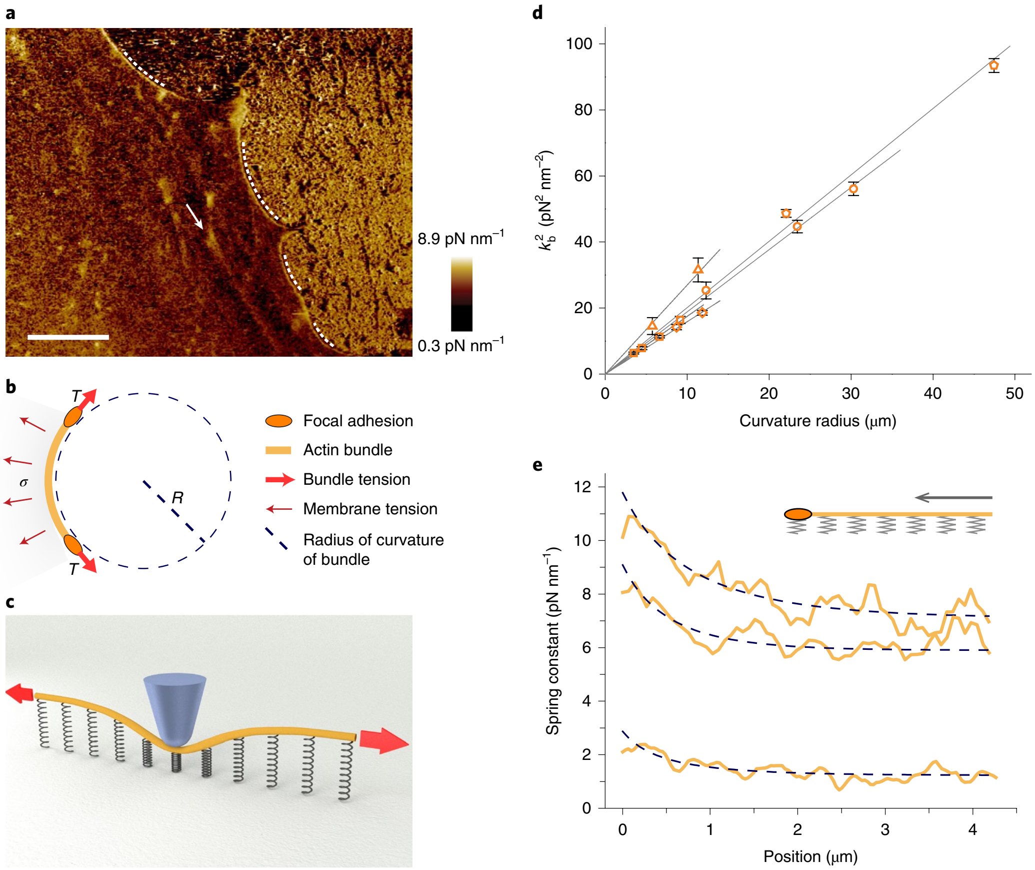

Fig. 3 | Cell stiffness patterns along actin bundles. **a**, Cell stiffness image of a living fibroblast. Dashed arcs and the white arrow highlight actin bundles. Scale bar, 5 μm. **b**, Schematic diagram of forces acting on a bundle at the cell edge. **c**, Illustration of the 1D model. The AFM tip (blue) is indenting the actin bundle (yellow rod) resting on distributed springs that represent the interaction of the bundle with the rest of the cell. Red arrows represent the direction of tension. **d**, Square of bundle stiffness versus curvature radius. Square, circle, diamond, triangle and pentagon symbols correspond respectively to cells i to v given in Supplementary Fig. 10. Error bars represent the noise in stiffness measurements, corresponding to mean ± s.e.m. determined from at least four repeated measurements on a given bundle. Solid lines show best linear fits. **e**, Stiffness profiles along bundles fitted with equation (8) (dashed lines). The lower curve is obtained from cell i and the top two curves are obtained from cell ii given in Supplementary Fig. 10.

with equation (8) gives l_b values of 1.4, 1.9 and 2.3 μm. Note that equation (1) and equation (2) can be solved for bundle tension. From the measured values of k_b and l_b, we find bundle tension values of 1.2, 2.8 and 8.2 nN. These values are close to estimates based on force–extension measurements of actin bundles extracted from cells[23] and traction forces exerted at focal adhesions[24].

While the model in Fig. 3c successfully predicts stiffness and stiffness gradients along actin bundles, it leaves out other regions of the cell. We therefore tested whether extending the underlying principle of this one-dimensional (1D) model to two dimensions can predict stiffness and stiffness gradients across the cortex of the cell. Described by a stretched sheet resting on an elastic foundation (Fig. 4a), the two-dimensional (2D) model has two parameters, σ_c and K_{2D}. σ_c corresponds to the cortex tension, which includes tension in the plasma membrane and the cortical actin. K_{2D} is the foundation modulus, and it can be related to the elastic modulus and thickness of the cytoplasm (see equation (10) in Methods). According to the 2D model, the stiffness, k_c, measured over the cortex depends mainly on the cortex tension through the following approximate relationship (see equation (11) in Methods for a more general relationship):

$$k_c \cong 2\sigma_c \tag{3}$$

On the other hand, the mechanical coupling distance over the cortex region, l_c, depends on both parameters:

$$l_c = \sqrt{\frac{\sigma_c}{K_{2D}}} \tag{4}$$

Equations (3) and (4) have testable predictions. First, from the measured values of k_c, equation (3) predicts cortex tension to be between 300 and 3,000 pN μm^{-1}. While it is difficult to measure cortex tension under the same conditions with an independent method, micropipette aspiration measurements provide an estimate. Measurements on mouse fibroblasts have yielded nominal cortex tension values around 400 pN μm^{-1}, and various drug treatments that inhibit or promote actomyosin contractility resulted in a range from approximately 150 to 1,900 pN μm^{-1} (ref. [25]). Second, the model accurately predicts spatial variation of stiffness (Fig. 4c,d), which is approximated well by the modified Bessel function of the second kind (see equation (13) in Methods). The values of l_c obtained by curve fitting vary from 250 to 1,000 nm, and correlate positively with σ_c (Fig. 4e), as anticipated from equation (4).

We additionally found that the 1D and 2D models can be unified due to the mechanical coupling between the bundles and the nearby regions of the cell. For example, when the AFM tip presses

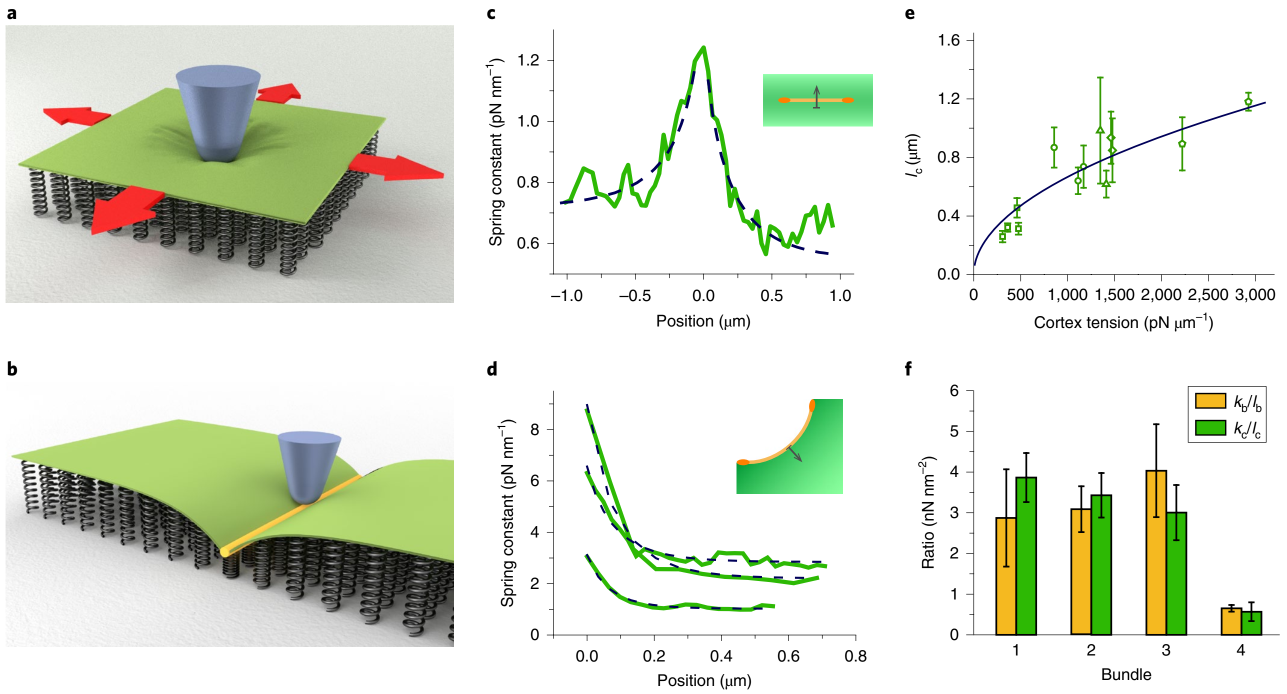

Fig. 4 | Cell stiffness patterns across the cortex. **a**, Illustration of the 2D model. The green surface represents the tensioned cell cortex and the plasma membrane. The AFM tip is shown in blue. The springs represent the stiffness of the cytoplasm. **b**, Illustration of the unified model. The yellow rod indicates an actin bundle. **c**,**d**, Representative stiffness gradients over the cortex, plotted perpendicular to a bundle away from the cell edge (**c**) and to three bundles at the edge (**d**). Insets illustrate the direction of the plots (arrows) relative to the actin bundles (yellow lines). Orange ellipses indicate focal adhesions. The entire dataset and the locations of measurements are given in Supplementary Fig. 10. Data are fitted with equation (13) in Methods (dashed curves). **e**, Coupling distances across the cortex versus cortex tension and the square-root relationship that fits the data. Square, circle, diamond, triangle and pentagon symbols correspond respectively to cells i to v given in Supplementary Fig. 10 along with the stiffness gradient plots used for estimating the coupling distances. **f**, Ratios of stiffness and coupling distances for bundles and cortices. Error bars in **e**,**f** correspond to the 68% confidence bound of estimated values, which approximates 1 s.d. in a normal distribution.

down on a bundle, forces would couple into the cortex up to a distance of approximately l_c (Fig. 4b). Hence, K_{1D} is related to K_{2D}, with $K_{1D} \cong K_{2D} l_c$ (and for bundles not on the edge $K_{1D} \cong 2K_{2D} l_c$). Rewriting this relationship in terms of experimentally observable parameters leads to

$$\frac{k_b}{l_b} \cong \frac{k_c}{l_c} \tag{5}$$

Evaluating the left- and right-hand sides of equation (5) for different actin bundles and their neighbouring cortices results in values that differ by less than 20% (Fig. 4f). To test the significance of this agreement, we evaluated equation (5) with parameters selected randomly from the dataset and found that fewer than 0.2% of the cases fall within the range seen in Fig. 4f ($P < 0.002$, Supplementary Note 2), suggesting that the agreement seen in Fig. 4f would be unlikely to occur if the parameters of equation (5) were uncorrelated. Importantly, equation (5) offers the possibility to determine l_b from measurements of k_b, k_c and l_c, which we found to be more broadly applicable than the curve fitting approach used in Fig. 3e, because the latter requires a steep gradient in stiffness along the bundle.

With the help of equations (1)–(5), and with measurements of k_b, k_c and l_c, we determined the magnitude of T across the bundles in all five fibroblast cells studied in Figs. 3 and 4, which are given in Fig. 5a, and σ_c near each bundle (Fig. 5b). In addition, by noting that K_{2D} in equation (4) depends on the elastic modulus and thickness of the cytoplasm through equation (10), we estimated the elastic modulus values of the cells (Fig. 5c), and found that they range from 0.3 to 0.6 kPa. While these values broadly agree with earlier measurements of elastic and shear moduli in cells[26,27], these earlier measurements were made at lower frequencies (see discussions in Supplementary Note 3).

In addition to the bundle and cortex tensions, it is also possible to estimate the plasma membrane tension, σ_m, of each cell, because σ_m is related to the tension and curvature radius of the actin bundles at the cell edge via the Laplace relationship[28]: $2\sigma_m = T/R$ (the factor 2 is due to the membranes in the basal and apical surfaces of the cell). This relationship is supported by observations that the curvature radius of actin bundles changes on myosin II inhibition, which were made with fibroblasts cultured on micropillar arrays[21], as well as with other cell types cultured on micropatterned substrates[22]. By substituting T in the Laplace relationship with experimentally observable parameters, σ_m can be written as

$$\sigma_m \cong \frac{k_b^2 l_c}{4Rk_c} \tag{6}$$

Because each curved bundle provides a different set of parameters (k_b, k_c, l_c and R), they allow multiple independent estimates of σ_m for each given cell. As shown by the ranges of values in Fig. 5d, these independent estimates provide consistent results at each cell, supporting equation (6), as well as equations (1)–(5), which we used to derive equation (6). Note that the measured plasma membrane tension values span a narrow range (105 to 191 pN μm^{-1}), which

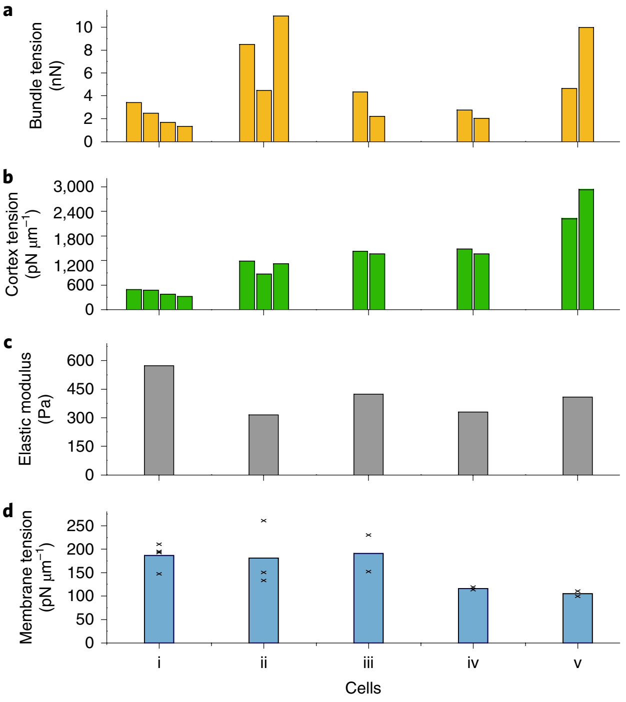

Fig. 5 | Measuring physiologically relevant intracellular forces from the stiffness images. a–d, Bundle tensions (**a**), cortex tensions (**b**), elastic moduli (**c**) and membrane tensions (**d**) of five fibroblast cells (i–v) calculated from the high-resolution stiffness images. The corresponding AFM images of each cell are given in Supplementary Fig. 10. In **a**,**b** each bar corresponds to a measurement from a distinct bundle and its adjacent cortical region. In **d** the cross symbols indicate independent measurements of membrane tension in each cell.

agrees with the notion that cells tightly regulate plasma membrane tension[29].

Altogether, our findings suggest a view of cell mechanical behaviour in which nanoscale mechanical properties are primarily determined by intracellular forces. A defining feature of this view is the coupling distance that determines how far the effects of a locally exerted force (for example with an AFM tip, or via cell–cell and cell–substrate mechanical interactions) is transmitted to the neighbouring regions of the cell. The mechanical coupling is mediated by the force-generating and transmitting cytoskeleton, and, as a result, AFM tips interact not only with the cellular material immediately below them, but also with regions separated from the contact point by a distance that depends on intracellular tensional prestress. This mechanical coupling may also have implications for force-dependent cellular processes such as rigidity sensing and adhesion, which involve forces exerted locally on the nanoscale, and depend on the stiffness of the cells near the adhesion zone[30]. In short, our analysis of cell stiffness at the nanoscale provides a mechanical model for the cell that links cell stiffness to physiologically relevant intracellular forces, and allows determination of these forces from cell stiffness images.

Online content

Any methods, additional references, Nature Research reporting summaries, source data, statements of code and data availability and associated accession codes are available at https://doi.org/10.1038/s41563-019-0391-7.

Received: 23 June 2016; Accepted: 30 April 2019;
Published online: 17 June 2019

References

1. Plodinec, M. et al. The nanomechanical signature of breast cancer. *Nat. Nanotechnol.* **7**, 757–765 (2012).
2. Stewart, M. P. et al. Hydrostatic pressure and the actomyosin cortex drive mitotic cell rounding. *Nature* **469**, 226–230 (2011).
3. Mammoto, T., Mammoto, A. & Ingber, D. E. Mechanobiology and developmental control. *Annu. Rev. Cell Dev. Biol.* **29**, 27–61 (2013).
4. Ingber, D. E. Mechanobiology and diseases of mechanotransduction. *Ann. Med.* **35**, 564–577 (2003).
5. Houk, A. R. et al. Membrane tension maintains cell polarity by confining signals to the leading edge during neutrophil migration. *Cell* **148**, 175–188 (2012).
6. Wirtz, D., Konstantopoulos, K. & Searson, P. C. The physics of cancer: the role of physical interactions and mechanical forces in metastasis. *Nat. Rev. Cancer* **11**, 512–522 (2011).
7. Fletcher, D. A. & Mullins, R. D. Cell mechanics and the cytoskeleton. *Nature* **463**, 485–492 (2010).
8. Zhu, C., Bao, G. & Wang, N. Cell mechanics: mechanical response, cell adhesion, and molecular deformation. *Annu. Rev. Biomed. Eng.* **2**, 189–226 (2000).
9. Ingber, D. E. Cellular tensegrity revisited I. Cell structure and hierarchical systems biology. *J. Cell Sci.* **116**, 1157–1173 (2003).
10. Oberleithner, H. et al. Potassium softens vascular endothelium and increases nitric oxide release. *Proc. Natl Acad. Sci. USA* **106**, 2829–2834 (2009).
11. Rotsch, C. & Radmacher, M. Drug-induced changes of cytoskeletal structure and mechanics in fibroblasts: an atomic force microscopy study. *Biophys. J.* **78**, 520–535 (2000).
12. Eghiaian, F., Rigato, A. & Scheuring, S. Structural, mechanical, and dynamical variability of the actin cortex in living cells. *Biophys. J.* **108**, 1330–1340 (2015).
13. Raman, A. et al. Mapping nanomechanical properties of live cells using multi-harmonic atomic force microscopy. *Nat. Nanotechnol.* **6**, 809–814 (2011).
14. Rigato, A., Rico, F., Eghiaian, F., Piel, M. & Scheuring, S. Atomic force microscopy mechanical mapping of micropatterned cells shows adhesion geometry-dependent mechanical response on local and global scales. *ACS Nano* **9**, 5846–5856 (2015).
15. Wang, A., Vijayraghavan, K., Solgaard, O. & Butte, M. J. Fast stiffness mapping of cells using high-bandwidth atomic force microscopy. *ACS Nano* **10**, 257–264 (2016).
16. Dong, M. D., Husale, S. & Sahin, O. Determination of protein structural flexibility by microsecond force spectroscopy. *Nat. Nanotechnol.* **4**, 514–517 (2009).
17. Brangwynne, C. P. et al. Microtubules can bear enhanced compressive loads in living cells because of lateral reinforcement. *J. Cell Biol.* **173**, 733–741 (2006).
18. Kumar, S. et al. Viscoelastic retraction of single living stress fibers and its impact on cell shape, cytoskeletal organization, and extracellular matrix mechanics. *Biophys. J.* **90**, 3762–3773 (2006).
19. Wang, N., Butler, J. P. & Ingber, D. E. Mechanotransduction across the cell-surface and through the cytoskeleton. *Science* **260**, 1124–1127 (1993).
20. Katoh, K., Kano, Y., Amano, M., Kaibuchi, K. & Fujiwara, K. Stress fiber organization regulated by MLCK and Rho-kinase in cultured human fibroblasts. *Am. J. Physiol. Cell Physiol.* **280**, C1669–C1679 (2001).
21. Rossier, O. M. et al. Force generated by actomyosin contraction builds bridges between adhesive contacts. *EMBO J.* **29**, 1055–1068 (2010).
22. Théry, M., Pepin, A., Dressaire, E., Chen, Y. & Bornens, M. Cell distribution of stress fibres in response to the geometry of the adhesive environment. *Cell Motil. Cytoskeleton* **63**, 341–355 (2006).
23. Deguchi, S., Ohashi, T. & Sato, M. Evaluation of tension in actin bundle of endothelial cells based on preexisting strain and tensile properties measurements. *Mol. Cell Biomech.* **2**, 125–133 (2005).
24. Ghibaudo, M. et al. Traction forces and rigidity sensing regulate cell functions. *Soft Matter* **4**, 1836–1843 (2008).
25. Tinevez, J. Y. et al. Role of cortical tension in bleb growth. *Proc. Natl Acad. Sci. USA* **106**, 18581–18586 (2009).
26. Mahaffy, R. E., Park, S., Gerde, E., Käs, J. & Shih, C. K. Quantitative analysis of the viscoelastic properties of thin regions of fibroblasts using atomic forcemicroscopy. *Biophys. J.* **86**, 1777–1793 (2004).
27. Fabry, B. et al. Time scale and other invariants of integrative mechanical behavior in living cells. *Phys. Rev. E* **68**, 041914 (2003).
28. Bar-Ziv, R., Tlusty, T., Moses, E., Safran, S. A. & Bershadsky, A. Pearling in cells: a clue to understanding cell shape. *Proc. Natl Acad. Sci. USA* **96**, 10140–10145 (1999).
29. Diz-Munoz, A., Fletcher, D. A. & Weiner, O. D. Use the force: membrane tension as an organizer of cell shape and motility. *Trends Cell Biol.* **23**, 47–53 (2013).

30. Gao, H., Qian, J. & Chen, B. Probing mechanical principles of focal contacts in cell–matrix adhesion with a coupled stochastic–elastic modelling framework. *J. R. Soc. Interface* **8**, 1217–1232 (2011).

Acknowledgements

We acknowledge M. P. Sheetz for helpful discussions, E. Bryant for help in setting up imaging and cell culture, T. Iskratsch and V. Stevenin for help with fibroblast culture and treatment, X. Chen for help with instrumentation, T. P. Stossel and F. Nakamura for providing M2 cells, L. Chasin for providing CHO cells and L. P. Alonso-Sarduy for culturing them. This work is supported by the NIH Director's New Innovator Award Program (1DP2-EB018657), the Rowland Fellows Program and the Wyss Institute for Biologically Inspired Engineering at Harvard University.

Author contributions

N.M. carried out AFM and fluorescence imaging and contributed to cantilever design, improvement of imaging protocols, data analysis and development of mechanical models. C.F. demonstrated proof of principle for the AFM imaging method and contributed to the development of imaging protocols. J.A.J.-M. contributed to the AFM and fluorescence imaging and to the development of mechanical models. K.V.T. contributed to AFM and florescence imaging, and development of imaging protocols. D.E.I. contributed to the development of mechanical models, experimental design and discussions. O.S. contributed to the cantilever design, development of mechanical models, experimental design and data analysis. O.S. and N.M. wrote the manuscript with input from all coauthors.

Competing interests

O.S. is a co-inventor on US Patents US7302833B2 and US7404314B2 assigned to Stanford University, which are related to the methods used this work. O.S. founded Big Apple Nano, Inc.

Additional information

Supplementary information is available for this paper at https://doi.org/10.1038/s41563-019-0391-7.

Reprints and permissions information is available at www.nature.com/reprints.

Correspondence and requests for materials should be addressed to O.S.

Methods

Cell cultures. M2 cells have been previously described[31] and were generously donated by T. P. Stossel, CHO cells were a generous gift from L. Chasin and HUVECs were acquired from Lonza. The aforementioned cell lines were grown according to the provider's instructions or standard culturing procedures. Mouse fibroblast cells (RPTPα$^{+/+}$ cell line, derived from E13–15 mouse embryos) have been previously described[32] and were generously donated by M. P. Sheetz. Fibroblasts were grown in basal DMEM (Life Technologies) supplemented with 10% fetal bovine serum (Atlanta Biologicals and Life Technologies) and 1% penicillin–streptomycin (Life Technologies) at 37 °C in a 5% CO_2 atmosphere. The final concentrations of penicillin and streptomycin were 30 mg l^{-1} and 50 mg l^{-1}, respectively. For experiments, fibroblasts were collected with 0.05% trypsin–EDTA (Life Technologies) and plated on fibronectin-coated dishes.

Live-cell imaging and analysis. To induce the expression of fluorescently tagged proteins, chemical transfection or viral transduction was used. In the first case, cells were transfected with Lifeact–GFP using standard chemical transfection reagents (Fugene 6, Promega) and imaged 2 to 3 d after transfection. In the second case, cells were transduced with baculoviruses harbouring the constructs actin–RFP, actin–GFP, talin–GFP and tubulin–GFP (Life Technologies) and imaged 1 to 2 d after transduction. Bright-field, phase and fluorescence images were acquired with an inverted epifluorescence fluorescence microscope (AxioObserver. A1, Zeiss) through a ×20 air or a ×100 oil-immersion objective. Images were captured with a standard CCD (charge-coupled device) camera (Hamamatsu). For fluorescence measurements, the camera dark noise was subtracted and cells that were high in fluorescence intensity were not included in the analysis. Alignment between fluorescence and AFM images was performed through the alignment of fiducial markers, such as stable cell edges and actin fibres. Data analysis was performed with built-in functions of the software ImageJ.

Torsional harmonic cantilevers. Custom T-shaped cantilevers were fabricated by conventional manufacturing protocols (Bruker-Nano). To image cells, cantilevers were either left uncoated or coated with a thin layer of silicon nitride. To perform coating, cantilevers were first treated with an ultraviolet/ozone cleaner (Bioforce Nanosciences), then coated with a thin (5 to 50 nm) layer of silicon nitride via plasma-enhanced chemical vapour deposition (Oxford Instruments). The deposited layer affected the cantilever thickness and spring constant. These changes were taken into account by cantilever calibration. Flexural—between 5 and 15 kHz—and torsional—approximately 100 kHz—resonance frequencies of cantilevers in liquid were determined from thermal noise spectra. Flexural and torsional deflection sensitivities of cantilevers were determined from ramp plots, assuming flexural and torsional motions to be described by springs in series. Flexural—approximately 200 pN nm^{-1}—and torsional—approximately 1 N m^{-1}—spring constants of cantilevers were determined from the amplitude of thermal vibrations. Cantilevers were imaged under a field emission scanning electron microscope (Agilent).

Cell preparation for experiments. Before the experiments, growth medium was replaced with fresh L-15 medium (Life Technologies) or complete DMEM with or without phenol red and HEPES (Life Technologies). Culture dishes were then mounted on the stage of a Bioscope II (Bruker) or Catalyst (Bruker) equipped with a Nanoscope V controller (Bruker) and imaged at ambient temperature. For myosin inhibition experiments, blebbistatin (EMD Millipore) was added to the culture dish to a final 100 µM concentration, then mixed thoroughly. For washout experiments, the drug-containing solution was removed by aspiration, and washout with fresh solution was performed at least seven times.

Atomic force microscopy. Cantilevers were driven in tapping mode close to their flexural resonance frequency as determined by the thermal noise spectrum. Tip–sample force waveforms were calculated in Labview (National Instruments) from the torsional signal, as previously described[33]. Only the first seven harmonics of the driving frequency were used to reconstruct the tip–sample force waveform. Imaging bandwidth was set by averaging consecutive force waveforms and was typically between 300 and 600 Hz. Force noise was determined from force fluctuations when the tip was not in contact with the surface. (Force waveforms in Fig. 1a were obtained at 100 Hz for clarity. As a result, they exhibited lower force noise than those obtained at 300–600 Hz.) The effective elastic modulus was calculated by fitting force versus distance curves with the DMT model[34], assuming a conical or hemispherical indenter. The curve fitting procedure assumed the contact point as a variable, which has been previously found to produce results close to the bulk properties in polymer-based samples[34]. The reduced dependence of the effective elastic modulus values on the contact point could be attributed in part to the speed of oscillations, which minimize drift during each force curve measurement, and the improved sensitivity of the torsional modes to tip–sample forces. These DMT-based effective elastic modulus values broadly agree with those generated by conventional force–distance curve methods acquired near the cell edge, but differ from those acquired near the cell centre (Supplementary Fig. 12). Note that these effective elastic modulus values were not included in the quantitative analysis of cellular stiffness patterns, which used spring constant values that were calculated from the slopes of force versus distance curves. All stiffness values are colour-coded in a logarithmic scale and are displayed either unmodified or after median filtering and removal of pores and spikes using Scanning Probe Image Processor (Image Metrology). Three-dimensional (3D) overlays of elastic modulus and topography were generated using the same software. To improve the clarity of these overlays, topography maps were flattened with line-wise and planar corrections, and spikes were removed.

Analysis of stiffness profiles. For the analysis of stiffness profiles at the curved cell edges (Fig. 3d), images of mouse fibroblast cells that have more than one curved edge with each edge displaying a long, narrow, stiff structure at the cell boundary were selected, as these features indicate the presence of a peripheral actin bundle (see Supplementary Fig. 10 for corresponding AFM images). These structures were stable at least for the duration of individual images, which were acquired within approximately 10 min. Supplementary Fig. 11 shows a sequence of images that display a cell edge that is acquiring curvature over time, but does not display a long, narrow, stiff structure at the cell boundary, and hence was not included in the analysis. The radius of curvature of the peripheral actin bundles was determined by fitting a circle through the coordinates of the bundle identified by the ImageJ plugin JFilament[35]. Stiffness profiles along actin bundles were obtained as a function of distance along the bundle. A 2 pixel by 2 pixel averaging sliding window was used to reduce noise. Pixels with negative spring constants were not included in the averaging. After determining the stiffness profiles, the values of k_b were obtained by averaging the spring constant values along each bundle. We excluded the measurements within about 0.5 µm of the ends of the bundles, as these values are affected by the focal adhesions due to mechanical coupling. The values of l_b were determined by fitting equation (8) to the stiffness profiles. A smoothing filter (Savitzky–Golay, order 1, side-points 2) was applied before displaying stiffness profiles to show the gradual increase in stiffness more clearly.

Stiffness profiles along the cortex near straight actin bundles were obtained by first averaging stiffness values along straight lines parallel to the actin bundle and then plotting them with respect to their distance from the bundle. Stiffness profiles near curved actin bundles were obtained by first averaging stiffness values along arcs with increasing radius of curvature and equal angular spread, and then plotting the averaged values with respect to the radius of curvature. Coupling distances were obtained by nonlinear curve fitting to equation (13) using the trust-region-reflective algorithm of MATLAB (MathWorks). Because equation (13) assumes only one bundle at the edge of an infinite cortex, we excluded regions that correspond to nearby bundles or focal adhesions in the curve fitting process by setting the corresponding weights to zero.

Stiffness of a tensioned beam over an elastic foundation. The balance of forces acting on the bundle leads to the following differential equation:

$$\frac{d^2 z}{dx^2} - \frac{K_{1D}}{T} z = 0 \tag{7}$$

Here z is the surface displacement as a function of position x. The solution to equation (1) is in the form $z = A\ e^{\pm x/l_b}$, with a characteristic decay length $l_b = \sqrt{T/K_{1D}}$. Using the boundary conditions $z(0) = h_{ind}$ and $z(\pm\infty) = 0$, the equation can be solved for the stiffness probed by the AFM tip at the origin $k(0) = 2\sqrt{K_{1D}T}$. In the case of a beam that is terminated at a boundary such as a focal adhesion, the stiffness profile seen by the AFM is

$$k_b(x) = \frac{2\sqrt{K_{1D}T}}{1 - \frac{m-1}{m} e^{-2x/l_b}} \tag{8}$$

Here x represents the distance from the boundary and m is the ratio of the stiffness measured at the boundary to the stiffness far away from the boundary ($x \gg l_b$). l_b can be determined by fitting this function to the stiffness values measured along a bundle near a focal adhesion.

Stiffness of a stretched sheet over an elastic foundation. The 2D model is represented by a sheet under surface tension σ_c that rests over an elastic foundation with foundation modulus K_{2D} (spring constant of a unit area). In cylindrical coordinates, the balance of forces acting on a ring of free surface leads to the following equation:

$$r\frac{d^2 z}{dr^2} + \frac{dz}{dr} - \frac{K_{2D}}{\sigma_c} r z = 0 \tag{9}$$

Here r is the radial distance from the AFM tip. Solutions to equation (3) involve the modified Bessel function of the second kind K_0: $z(r) = \beta K_0(r/l_c)$, with a characteristic decay length $l_c = \sqrt{\sigma_c/K_{2D}}$. Note that, since tensional forces are accounted for in the model by σ_c, K_{2D} can be viewed as the stiffness of the tension-free cytoplasm. As an approximation, if the thickness of the cytoplasm h is less than l_C, K_{2D} can be related to the elastic modulus E of the tension-free cytoplasm by

$$K_{2D} \cong E/h \tag{10}$$

The boundary condition at the tip can be approximated in different ways with varying degrees of accuracy. The case for the flat punch indenter with radius *a* leads to a simple approximate expression for the stiffness:

$$k_\mathrm{c} \cong \frac{2\pi\sigma_\mathrm{c}}{K_0(a/l_\mathrm{c})} \qquad (11)$$

Although stiffness depends on the ratio a/l_c, the relationship is weak. For *a* around 10 to 100 nm, $k_\mathrm{c} \cong 2\sigma_\mathrm{c}$ serves as a good approximation. Note that the results in Fig. 3 were obtained with spherical AFM tips with approximately 60 nm radii.

In the presence of a bundle, circular symmetry is broken. However, the stiffness can still be determined by noting the boundary condition imposed by the bundle: $Tz_{yy} = \sigma_c z_x$. Here z_x and z_{yy} are the first and second derivatives of surface displacement in the directions perpendicular to and along the bundle respectively. The resulting change in stiffness as the tip approaches a bundle at the cell edge can be determined numerically from the following equation:

$$k_\mathrm{c}^{-1}(x) - k_\mathrm{c}^{-1}(\infty) = \frac{1}{(2\pi)^2\sigma_\mathrm{c}} \int_{-\infty}^{+\infty} \frac{2\omega^2 F^2(K_0(\sqrt{x^2+y^2}/l_\mathrm{c}))}{\omega^2 F(K_0(y/l_\mathrm{c})) + \pi\sigma_\mathrm{c}/T} \mathrm{d}\omega \qquad (12)$$

Here $F(K_0(y/l_c))$ represents the Fourier transform for the independent variable *y* and ω is the Fourier transform variable. We found that the numerically determined stiffness variation is approximated well by the following relationship:

$$k_\mathrm{c}(x) \cong \beta K_0(4x/l_\mathrm{c}) + k_\mathrm{c}(\infty) \qquad (13)$$

Therefore, for simplicity, l_c was determined by fitting stiffness data in Fig. 4c,d with this function. Note that experimentally the origin ($x = 0$) is not defined. We chose the origin as either the position of the peak stiffness or the next highest value if the stiffness value plateaued near the peak, which could happen if the bundle is wider than the width of a single pixel. Furthermore, to avoid the singularity of the modified Bessel function at the origin, we offset the position of the measurements by 30 nm, which corresponds to the nominal contact diameter.

Reporting Summary. Further information on research design is available in the Nature Research Reporting Summary linked to this article.

Data availability

All the data supporting the findings of this study are available within the article or its Supplementary Information files, or from the corresponding authors on reasonable request.

References

31. Cunningham, C. C. et al. Actin-binding protein requirement for cortical stability and efficient locomotion. *Science* **255**, 325–327 (1992).
32. Su, J., Muranjan, M. & Sap, J. Receptor protein tyrosine phosphatase alpha activates Src-family kinases and controls integrin-mediated responses in fibroblasts. *Curr. Biol.* **9**, 505–511 (1999).
33. Sahin, O., Magonov, S., Su, C., Quate, C. F. & Solgaard, O. An atomic force microscope tip designed to measure time-varying nanomechanical forces. *Nat. Nanotechnol.* **2**, 507–514 (2007).
34. Sahin, O. & Erina, N. High-resolution and large dynamic range nanomechanical mapping in tapping-mode atomic force microscopy. *Nanotechnology* **19**, 445717 (2008).
35. Smith, M. B. et al. Segmentation and tracking of cytoskeletal filaments using open active contours. *Cytoskeleton* **67**, 693–705 (2010).

nature research

Corresponding author(s): Ozgur Sahin

Reporting Summary

Nature Research wishes to improve the reproducibility of the work that we publish. This form provides structure for consistency and transparency in reporting. For further information on Nature Research policies, see Authors & Referees and the Editorial Policy Checklist.

Statistical parameters

When statistical analyses are reported, confirm that the following items are present in the relevant location (e.g. figure legend, table legend, main text, or Methods section).

n/a	Confirmed	
☐	☒	The exact sample size (*n*) for each experimental group/condition, given as a discrete number and unit of measurement
☐	☒	An indication of whether measurements were taken from distinct samples or whether the same sample was measured repeatedly
☒	☐	The statistical test(s) used AND whether they are one- or two-sided *Only common tests should be described solely by name; describe more complex techniques in the Methods section.*
☒	☐	A description of all covariates tested
☒	☐	A description of any assumptions or corrections, such as tests of normality and adjustment for multiple comparisons
☐	☒	A full description of the statistics including central tendency (e.g. means) or other basic estimates (e.g. regression coefficient) AND variation (e.g. standard deviation) or associated estimates of uncertainty (e.g. confidence intervals)
☐	☒	For null hypothesis testing, the test statistic (e.g. *F*, *t*, *r*) with confidence intervals, effect sizes, degrees of freedom and *P* value noted *Give P values as exact values whenever suitable.*
☒	☐	For Bayesian analysis, information on the choice of priors and Markov chain Monte Carlo settings
☒	☐	For hierarchical and complex designs, identification of the appropriate level for tests and full reporting of outcomes
☒	☐	Estimates of effect sizes (e.g. Cohen's *d*, Pearson's *r*), indicating how they were calculated
☐	☒	Clearly defined error bars *State explicitly what error bars represent (e.g. SD, SE, CI)*

Our web collection on statistics for biologists may be useful.

Software and code

Policy information about availability of computer code

Data collection	Atomic Force Microscope images were collected by the Nanoscope software (version 9.1, by Bruker-Nano, Inc.). Cantilever deflection signals were collected using LabVIEW (version 2012, by National Instruments).
Data analysis	Curve fitting was done using built in functions in Matlab (versions 8.1 and 9.1, by Mathworks). Locations of bundles studied in Fig. 3 and Supp. Fig. 10 were determined by the JFilament plugin in ImageJ. Scanning Probe Image Processor (SPIP, version 5, by Image Metrology A/S) was used to perform flattening, line wise and planar corrections, median filtering, pore and spike removal of effective elastic modulus images, and 3-D rendering of AFM topography with overlays of effective elastic modulus images.

For manuscripts utilizing custom algorithms or software that are central to the research but not yet described in published literature, software must be made available to editors/reviewers upon request. We strongly encourage code deposition in a community repository (e.g. GitHub). See the Nature Research guidelines for submitting code & software for further information.

Data

Policy information about availability of data

All manuscripts must include a data availability statement. This statement should provide the following information, where applicable:

- Accession codes, unique identifiers, or web links for publicly available datasets
- A list of figures that have associated raw data
- A description of any restrictions on data availability

All the data supporting the findings of this study are available within the article, its Supplementary Information files, or from the corresponding authors upon reasonable request.

Field-specific reporting

Please select the best fit for your research. If you are not sure, read the appropriate sections before making your selection.

☒ Life sciences ☐ Behavioural & social sciences

For a reference copy of the document with all sections, see nature.com/authors/policies/ReportingSummary-flat.pdf

Life sciences

Study design

All studies must disclose on these points even when the disclosure is negative.

Sample size	Sample sizes were limited by the number of curved actin fiber bundles observed in the atomic force microscope images of a given cell edge. In the five biological replicates, sample sizes were 4, 3, 2, 2, and 2, respectively. Because the prediction being tested was a specific mathematical relationship between stiffness and curvature (Equation 1), a minimum of two samples were sufficient to test the hypothesis.
Data exclusions	No data were excluded from the analysis.
Replication	All attempts at replication were successful. First, Equation 1 was tested with measurements from the bundles of the cell displayed in Figure 3a. Replications were attempted with samples from other cells that display a minimum of two curved stiff structures near the edge of the cell. Observation of stiff structures ensures that the bundle is present and the AFM can detect the stiffness of the bundle, so the equation becomes testable.
Randomization	The study did not compare groups of samples, therefore randomization was not used.
Blinding	Experiments did not involve group allocation, therefore blinding was not used.

Materials & experimental systems

Policy information about availability of materials

n/a	Involved in the study
☒	☐ Unique materials
☒	☐ Antibodies
☐	☒ Eukaryotic cell lines
☒	☐ Research animals
☒	☐ Human research participants

Eukaryotic cell lines

Policy information about cell lines

Cell line source(s)	Mouse Fibroblast cells (RPTP-α+/+ cell line) were donated by M. P. Sheetz, who obtained them originally from J. Sap. M2-melanoma cells were donated by M.P. Sheetz, who obtained them originally from T. P. Stossel. Chinese Hamster Ovary (CHO-K1) cells were provided by Larry Chasin, Dept. of Biological Sciences, Columbia University, who in turn brought them to his lab in 1970 from the laboratory of their origin, that of Theodore Puck and Fa-ten Kao at the University of Colorado Medical School Human Umbilical Vein Endothelial cells are obtained from Lonza.
Authentication	Mouse fibroblast cell line was authenticated by the source lab using genetic evaluation for intraspecies contamination and mouse STR profile (Authentication date: July 03/2018). No authentication was done for the remaining cell lines (M2-Melanoma, Chinese Hamster Ovary, and Human Umbilical Vein Endothelial Cells).
Mycoplasma contamination	Mouse Fibroblast cells were tested negative for mycoplasma contamination. Remaining cell lines (M2, CHO, HUVEC) were not

Mycoplasma contamination	tested for mycoplasma contamination.
Commonly misidentified lines (See ICLAC register)	No commonly misidentified cell lines were used.

Method-specific reporting

n/a	Involved in the study
☒	☐ ChIP-seq
☒	☐ Flow cytometry
☒	☐ Magnetic resonance imaging